Photophysics of Octabutoxy Phthalocyaninato-Ni(II) in Toluene: Ultrafast Experiments and DFT/TDDFT Studies

Tissa C. Gunaratne,[†] Alexey V. Gusev,[†] Xinzhan Peng,[‡] Angela Rosa,*[,§] Giampaolo Ricciardi,*[,§] Evert Jan Baerends,[||] Corrado Rizzoli,[⊥] Malcolm E. Kenney,*[,‡] and Michael A. J. Rodgers*[,†]

Contribution from The Center for Photochemical Sciences and Department of Chemistry, Bowling Green State University, Bowling Green, Ohio 43403, The Department of Chemistry, Case Western Reserve University, Cleveland, Ohio 44106, Dipartimento di Chimica, Università della Basilicata, Via N. Sauro 85, 85100 Potenza, Italy, Afdeling Theoretische Chemie, Vrije Universiteit, De Boelelaan 1083, 1081 HV Amsterdam, The Netherlands, and Dipartimento di Chimica Generale ed Inorganica, Università di Parma, Viale delle Scienze, 43100 Parma, Italy

Received: September 19, 2004; In Final Form: December 10, 2004

Reported herein is a combination of experimental and DFT/TDDFT theoretical investigations of the ground and excited states of 1,4,8,11,15,18,22,25-Octabutoxyphthalocyaninato-nickel(II), NiPc(BuO)$_8$, and the dynamics of its deactivation after excitation into the $S_1(\pi,\pi^*)$ state in toluene solution. According to X-ray crystallographic analysis NiPc(BuO)$_8$ has a highly saddled structure in the solid state. However, DFT studies suggest that in solution the complex is likely to flap from one D_{2d}-saddled conformation to the opposite one through a D_{4h}-planar structure. The spectral and kinetic changes for the complex in toluene are understood in terms of the 730 nm excitation light generating a primarily excited S_1 (π,π^*) state that transforms initially into a vibrationally hot $^3(d_{z^2},d_{x^2-y^2})$ state. Cooling to the zeroth state is complete after ca. 8 ps. The cold (d,d) state converted to its daughter state, the ^{3}LMCT ($\pi,d_{x^2-y^2}$), which itself decays to the ground state with a lifetime of 640 ps. The proposed deactivation mechanism applies to the D_{2d}-saddled and the D_{4h}-planar structure as well. The results presented here for NiPc(BuO)$_8$ suggest that in nickel phthalocyanines the ^{1,3}LMCT ($\pi,d_{x^2-y^2}$) states may provide effective routes for radiationless deactivation of the $^{1,3}(\pi,\pi^*)$ states.

Introduction

Metallophthalocyanines (MPcs) have been studied extensively since the beginning of the century. These highly stable macrocyclic π systems display interesting properties such as light stability and efficient light absorption in the near-UV/visible/near-IR region of the spectrum that make them potential candidates for applications in high-tech fields, including molecular electronics, nonlinear optics, liquid crystals, and photovoltaic solar cells.[1−3] Owing to the intense absorption in the near-IR region, which coincides with the therapeutic window where tissue absorption and scattering is minimal, metallophthalocyanines have been extensively used as photodynamic reagents for cancer therapy and other medical applications.[4,5] Recently there has been increased interest in metallophthalocyanines as photothermal sensitizers for tumor therapy purposes due to the promising results obtained for Ni(II)5,9,14,18,23,27,32,36-octabutoxy-2,3-naphthalocyanine, NiNc(BuO)$_8$.[6] This compound has been found to meet the conditions for the photothermal process to be effective, viz., it shows efficient absorption of the photon energy and rapid deactivation to produce highly localized thermal effects that can subsequently lead to cell death. To rationalize the factors governing the efficiency of the photothermal behavior of NiNc(BuO)$_8$, the knowledge of the excited-state dynamics is essential. However, to the best of our knowledge, no studies on the fundamental deactivation processes of nickel phthalocyanines have been reported in the literature.

Previous studies on the photophysical properties of nickel tetrapyrroles have mainly focused on nickel porphyrins (see ref 7 and references therein). Similar to NiNc(BuO)$_8$, nickel porphyrins in noncoordinating solvents show rapid radiationless decay of the primarily excited (π,π^*) state. Nickel(II) porphyrins have a d^8 metal electronic configuration, so in the absence of axial ligands, the d_{z^2} orbital is the highest filled metal orbital and the $d_{x^2-y^2}$ orbital is empty. The lack of luminescence, together with results of extended Hückel calculations, has led to the proposal that the normally emissive $^{1,3}(\pi,\pi^*)$ excited states of the porphyrin ring deactivate rapidly via low-energy $^{1,3}(d_{z^2},d_{x^2-y^2})$ states.[8,9] Indeed, ultrafast absorption measurements of common nickel porphyrins such as NiTPP and NiOEP have revealed that a (d,d) state forms within <1 ps,[10−12] followed by deactivation to the ground state in 200−500 ps.[13−19] The excited state relaxation processes in such molecules are highly complex since they display photoinduced transient nuclear dynamics. For example, the transient optical bands of the (d,d) excited state in noncoordinating media narrow and blue-shift with wavelength-dependent kinetics on the 5−25 ps time scale.[10−12] This complex spectral evolution has been described in terms of vibrational relaxation (cooling) of the hot metal centered state.

The deactivation mechanism proposed for nominally planar nickel porphyrins in noncoordinating solvents cannot be tout

* To whom correspondence should be addressed.
[†] Bowling Green State University.
[‡] Case Western Reserve University.
[§] Università della Basilicata.
[||] Vrije Universiteit.
[⊥] Università di Parma.

10.1021/jp0457444 CCC: $30.25
Published on Web 02/19/2005

court translated to nickel phthalocyanines since the differences in the macrocyclic framework result in significant changes in the orbital level pattern.[20−22] Worth mentioning in this context are (i) the reduced G-a_{1u}/G-eg* (G = Gouterman) energy gap due to the destabilization of the G-a_{1u} induced by the benzo rings and (ii) the increased $d_{z^2}/d_{x^2-y^2}$ energy gap due to the upshift of the $d_{x^2-y^2}$ related to the contraction of the coordination cavity. Thus, on going from nickel porphyrin to nickel phthalocyanine, the $S_1(\pi,\pi^*)$ state moves to longer wavelengths and the $^{1,3}(d_{z^2},d_{x^2-y^2})$ ligand field excited states move to shorter wavelengths to the effect that the $^{1,3}(d_{z^2},d_{x^2-y^2})$ ligand field excited states which are central intermediates in the deactivation of photoexcited low-spin d^8 nickel porphyrins, might not be involved at all in the radiationless decay of nickel phthalocyanines. Instead, a relevant role in the deactivation of photoexcited low-spin d^8 nickel phthalocyanines might be played by LMCT states. Indeed, due to the upshift of the G-a_{1u}, the ^{1,3}LMCT states involving excitation out of the G-a_{1u} into the Ni-$d_{x^2-y^2}$ MOs might be low enough in energy to provide effective routes for deactivation of the normally emissive $^{1,3}(\pi,\pi^*)$ states.

It is the aim of this paper to provide the first experimental and theoretical investigation of the static and dynamic photophysical properties of nickel phthalocyanines, using Ni(II)1,4,8,-11,15,18,22,25-octabutoxy-phthalocyanine, $NiPc(BuO)_8$, as a case study.

The peripheral butoxy groups impart high solubility to this molecule in common organic solvents and, most importantly, induce a red-shift of the Q-band by ca. 70 nm relative to the unsubstituted analogue, which makes $NiPc(BuO)_8$ suitable for use as photothermal sensitizer. The complex has been resynthesized and structurally characterized through X-ray crystallography, and its excited-state spectral and dynamic behavior in a noncoordinating solvent (toluene) has been studied by ultrafast transient absorption spectroscopy and DFT/TDDFT calculations.

Experimental Section

Materials. *$NiPc(BuO)_8$.* Under Ar, a mixture of $H_2Pc(BuO)_8$ (173 mg, 0.158 mmol), $Ni(CH_3CO_2)_2{\cdot}4H_2O$ (1.51 g, 6.07 mmol), and dimethylformamide (30 mL) was refluxed for 1.5 h and evaporated to dryness by rotary evaporation (45 °C). The solid was chromatographed twice (basic Al_2O_3 III, ethyl acetate-toluene, 1:2), further chromatographed (Bio-Beads S-X1 (Bio-Rad Laboratories, Hercules, CA), toluene), dissolved in CH_2Cl_2 (5 mL), recovered with CH_3OH (15 mL), washed (CH_3OH), vacuum-dried (room temperature), and weighed (87 mg, 48%). UV−vis (toluene) λ_{max}, nm (log ϵ): 732 (5.42). NMR ($CDCl_3$): δ 7.50 (s, 2,3,9,10,16,17,23,26-Ar H), 4.78 (t, OR-1 CH_2), 2.19 (m, OR-2 CH_2), 1.64 (m, OR-3 CH_2), 1.07 (t, OR-4 CH_3). MS−HR−FAB exact mass *m*/*z*: calcd for $C_{64}H_{81}N_8{}^{58}NiO_8$ $(M+H)^+$, 1147.5530; found, 1147.5529, 1147.5527. The compound is a green solid. It is soluble in CH_2Cl_2 and toluene, and slightly soluble in hexanes.

X-ray Crystallography. Crystal data and details associated with structure refinement are given in Table 1 and in the Supporting Information. Data were collected on a Bruker AXS 100 CCD diffractometer using graphite-monochromatized Mo Kα radiation at 298 K. A total of 1206 frames were collected with a $\Delta\omega$ of 0.3 degrees and an exposition time of 20 s. Solution and refinement were carried out using the programs SIR97[23] and SHELX93.[24]

UV−Visible Absorption Spectra. The ground-state absorption spectra were recorded for $Ni(II)Pc(BuO)_8$ (2−3 μM) in toluene solutions using a Varian Cary 50 Bio single beam spectrophotometer.

TABLE 1: Experimental Data for the X-ray Diffraction Study on Crystalline $NiPc(BuO)_8$

complex	$NiPc(BuO)_8$
formula	$C_{64}H_{80}N_8NiO_8$
a, Å	14.107(1)
b, Å	14.121(1)
c, Å	16.871(1)
α,°	86.52(1)
β,°	72.52(1)
γ,°	73.30(1)
V, Å^3	3069.2(4)
Z	2
formula weight	1148.10
space group	$P\bar{1}$ (n. 2)
t, °C	25
λ, Å	0.71073
ρ_{calc}, g cm^{-3}	1.242
μ, cm^{-1}	3.76
transmission coefficient	0.903−0.978
R[a]	0.066
wR_2	0.172
GOF	1.09
N-observed[b]	6264
N-independent[c]	13767
N-refinement[d]	7120
variables	712

[a] Calculated on the observed reflections having $I > 2\sigma(I)$. [b] *N*-observed is the number of the independent reflections having $I > 2\sigma(I)$. [c] *N*-independent is the number of independent reflections. [d] *N*-refinement is the number of reflection used in the refinement having $I > 1.5\sigma(I)$.

Ultrafast Pump−Probe Measurements. The pump−probe instrument for ultrafast transient absorption measurements has been described previously.[25] The recent improvements to enhance signal-to-noise characteristics have been communicated elsewhere.[26] In the current experiments, the excitation wavelengths at 660 and 730 nm were generated with an optical parametric amplifier (OPA 800, Spectra Physics), pumped with 800 nm light from an amplified, mode-locked Ti:Sapphire laser (Hurricane, Spectra-Physics).

Cyclic Voltammetry and Spectro-Electrochemistry Experiments. Electrochemical oxidations and reductions (controlled-potential coulometry) were carried out using a Bioanalytical Systems Epsilon unit. A standard three electrode system was used except in the case of nonaqueous solvents where a silver wire was used as the reference electrode. Tetramethylammonium hexafluorophosphate was the supporting electrolyte. A home-made spectro-electrochemical cell was employed. This cell consisted of a screw cap 0.5 mm path length rectangular quartz cuvette attached into a Teflon beaker. Platinum gauze, 100 mesh, woven from 0.07 mm diameter platinum wire was used as the semitransparent working electrode. The electrode was placed in the 0.5 mm spectrophotometric cell and connected to the potentiostat output by a platinum wire. The potential applied to the electrode produced oxidized or reduced species that diffused away from the wire electrode to saturate the 0.5 mm layer of solution inside the spectrophotometric cell. The absorption spectra (HP 8453 UV−visible spectrophotometer) of the sample were taken until the potential-induced spectral evolution was complete. The spectro-electrochemical cell filled with pure solvent was used as reference.

Computational Details and Theoretical Methods. All calculations were performed with the ADF (Amsterdam Density Functional) suite of programs, release 2004.01.[27−29]

The calculations made use of the local density approximation (LDA) functional of Vosko−Wilk−Nusair (VWN),[30] plus the generalized gradient approximation (GGA), employing Becke's[31]

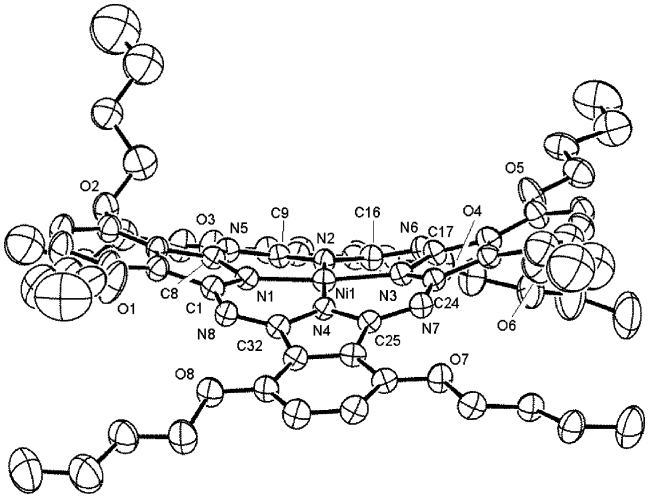

Figure 1. ORTEP side view (30% probability ellipsoids) of complex $NiPc(BuO)_8$. Disorder affecting some butyl chains has been omitted for clarity.

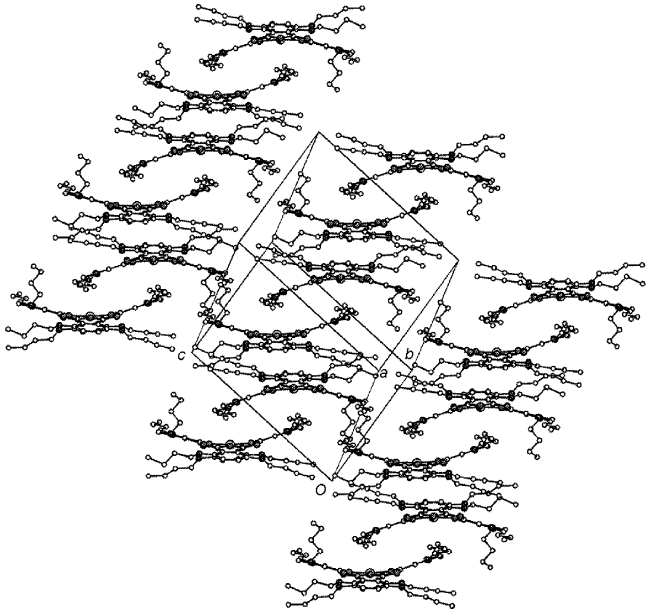

Figure 2. SCHAKAL view of the packing along the [1−1 0] direction.

gradient approximation for exchange and Perdew's[32] for correlation. The excitation energies were calculated using time-dependent density functional theory (TDDFT). In the ADF implementation,[33,34] the solution of the TDDFT response equations proceeds in an iterative fashion starting from the usual ground state or zeroth-order Kohn−Sham (KS) equations.[34] For these, one needs an approximation to the usual static exchange-correlation (xc) potential υ_{xc} (**r**). After the ordinary KS equations have been solved, the first-order density change has to be calculated from an iterative solution to the first-order KS equations. In these first-order equations, an approximation is needed to the first functional derivative of the time-dependent xc potential $\upsilon_{xc}(\mathbf{r}, t)$ with respect to the time-dependent density $\rho(\mathbf{r}', t')$, the so-called xc kernel. For the xc kernel, we used the adiabatic local density approximation (ALDA). In this approximation, the time dependence (or frequency dependence referring to the Fourier transformed kernel) is neglected, and one simply uses the differentiated static LDA expression. In our case the VWN parametrization was used.[30] For the exchange-correlation potentials which appear in the zeroth-order KS equations, we employed the same GGA as in the DFT calculations.

To facilitate the calculations on the title compound, a model compound, $NiPc(MeO)_8$ (Me = methyl), was chosen in which the butyl substituents were replaced by methyl groups. Geometry optimizations were performed for the ground and selected triplet excited states of the model system. Open-shell DFT calculations for the triplets were carried out using the unrestricted formalism. The ADF TZ2P basis set, which is an un-contracted triple-ζ STO basis set with one 3d and one 4f polarization function for C, N, and O atoms, one 2p and one 3d polarization function for H, and a triple-ζ 3d, 4s basis with one 4p and one 4f function for Ni, was used. The cores (C, N, O, 1s; Ni, 1s−2p) were kept frozen.

The molecular orbitals were visualized with Molden3.6[35] and the ADF output data were converted to Molden format using the ADF2MOLDEN program.[36]

Results and Discussion

X-ray Structure of $NiPc(BuO)_8$. The experimentally determined crystal structure of $NiPc(BuO)_8$ is shown in Figure 1. Selected bond distances, angles, and metrical parameters are quoted in Table 1.

The structural data reveal that the macrocycle assumes a saddle conformation, with the indole rings tilted alternately up and down, almost as rigid bodies. The dihedral angles, formed by the mean planes through the indole rings and the phthalocyanine mean plane are 15.4(1)°, 16.5(1)°, 16.0(1)°, and 16.1(1)° for the indole rings associated to the N(1), N(2), N(3), and N(4) atoms, respectively. The opposite N(1), C(1)···C(8), N(3), C(17)···C(24) and N(2), C(9)···C(16), N(4), C25)···C(32) form dihedral angles of 31.5(1)° and 32.4(1)° respectively.

The average absolute perpendicular displacement from the phthalocyanine mean plane of the pyrrolic N and C_β atoms, $|\Delta N_p|$ and $|\Delta C_\beta|$, and the meta carbon atoms of the benzo rings, $|\Delta C_m|$, are 0.109(4), 0.670(5), and 1.319(6) Å respectively.

The structural data also revealed a gentle sideway tilt (ruffling) of the indole rings superimposed on the quite large vertical tilt. The molecular parameters that define the degree of ruffling, i.e., the average transannular dihedral angle $(C_\alpha N_p N_p C_\alpha)_{op}$ and the average out-of-plane displacement of the *meso*-nitrogen atoms from the phthalocyanine mean plane, $|\Delta N_{meso}|$, amount to only 2.9(6)° and 0.056(4) Å, respectively.

The N_4 core shows a small but significant tetrahedral distortion ranging from −0.110(4) Å for N(2) to 0.110(4) Å for N(1), the metal being displaced by 0.002(1) Å from the least-squares plane through it. The $Ni-N_p$ bond distances (mean value 1.878(4) Å) are not remarkably different from each other and a little (but significantly) shorter than those reported in the literature for Ni-phthalocyanine complexes (mean value 1.904(18) Å calculated over four entries from the Cambridge Crystallographic Data File).[37−40]

The N−C and C−C bond distances are, as expected, consistent with a complete delocalization within the macrocycle. As for the C_o-O bond distances, they are indicative of a not negligible conjugation between the oxygen lone pairs and the phthalocyanine π system. The extent of the conjugation, however, depends significantly on the displacement of the C_{but} atoms from the mean plane through the benzene moiety of the corresponding indole ring that ranges from 0.078(6) to 1.209(12) Å, the mean value being 0.34(12) Å.

In the crystal packing, the molecules are disposed in layers parallel to the [1−1 0] direction (Figure 2) in such a way that each molecule arranges the butyl chains as guests of the cavities of over- and under-imposed layers, acting in the same time as

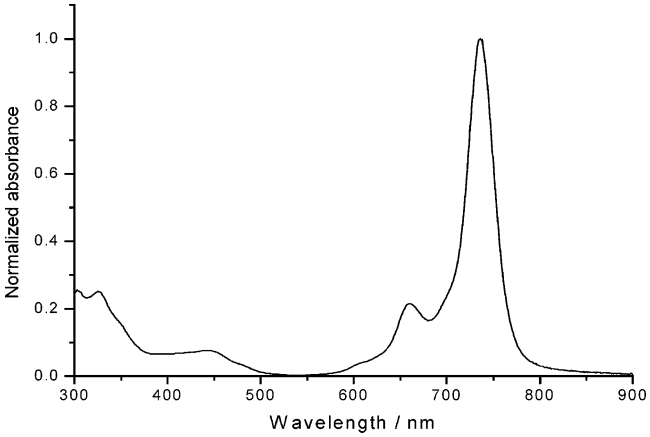

Figure 3. Optical absorption spectrum of NiPc(BuO)$_8$ in toluene.

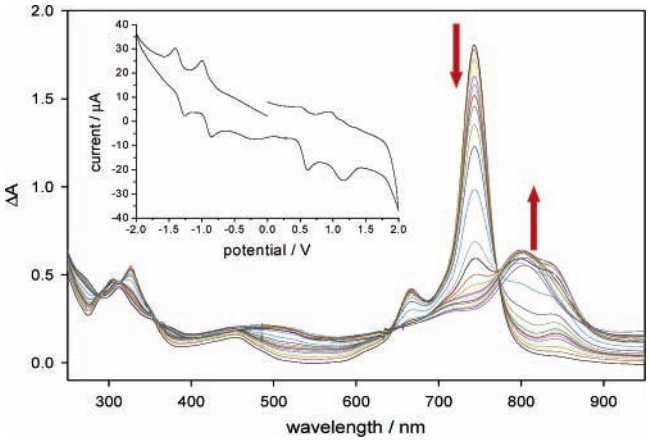

Figure 4. Progress over 25 min of spectro-electrochemical oxidation of NiPc(BuO)$_8$ (10μM) in CH_2Cl_2 at a constant potential of +500 mV. Inset: a cyclic voltammetry scan of the same solution showing two oxidation and two reduction waves.

a guest for the butyl chains of adjacent molecules. In this arrangement some C−H···O and CH−N contacts involving the C atoms from the butyl chains could be interpreted in terms of weak hydrogen interaction, the shortest one being C(42)B··· O(4)′, 3.344(13) Å; H(424)···O(4)′, 2.60 Å; C(42)B−H(424)··· O(4)′, 133.8° C(42)B···N(6)′, 3.580(14) Å; H(424)···N(6)′, 2.76 Å; C(42)B−H(424)···N(6)′, 142.7° C(58)···O(8)″, 3.546-(7) Å; H(582)···O(8)″, 2.67 Å; C(58)−H(582)···O(8)″, 150.4° (the prime and double primes refer to transformations of $-x$, 1 $-$ y, 1 $-$ z and 1 $-$ x, $-y$, 1 $-$ z, respectively).

Ground-State Spectrum. The ground state absorption spectrum recorded in toluene at room temperature is shown in Figure 3. In the energy window of interest for the present study, it shows two clear vibrational progression peaks corresponding to the Q(1,0) and Q(0,0) bands and a broad absorption immediately to the blue of the Q(1,0) vibronic band. Comparison of the visible absorption spectra of NiPc(BuO)$_8$ and NiPc reveals that the butoxy groups at the ortho positions cause a substantial red shift (more than 70 nm) of the Q(0,0) band of NiPc(BuO)$_8$ and introduce additional absorptions to the blue of the Q(1,0) band.

Voltammetric and Spectro-Electrochemistry Experiments. Figure 4 shows the results of spectro-electrochemical oxidation of compound I (10 μM) in dichloromethane solution. The potential was held constant at 500 mV and the spectra were recorded at times in the range of 0−25 min. At the end of the oxidation sequence, the neutral compound (λ_{max} = 730 nm) was seen to be wholly converted into the oxidized form. The inset

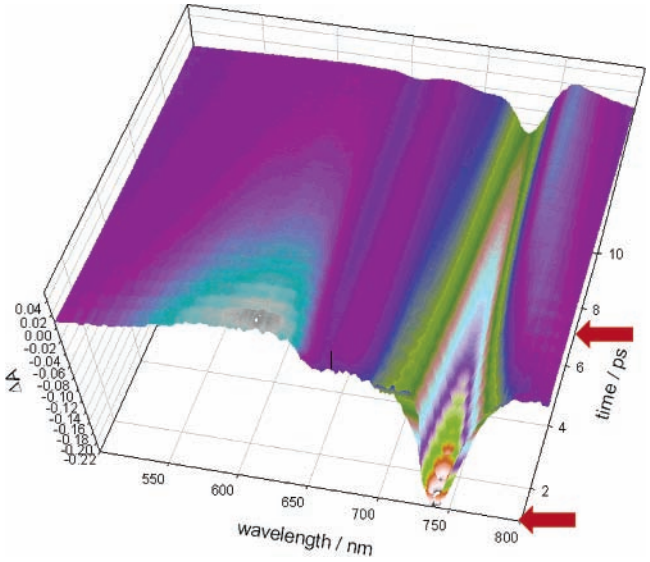

Figure 5. Perspective view of the first 10 ps of the A(λ, t) surface collected during an ultrafast pump−probe experiment with 10 μM NiPc-(BuO)$_8$ in toluene excited at 740 nm. The red arrows indicate the times of the first two of the spectral cuts shown in Figure 6.

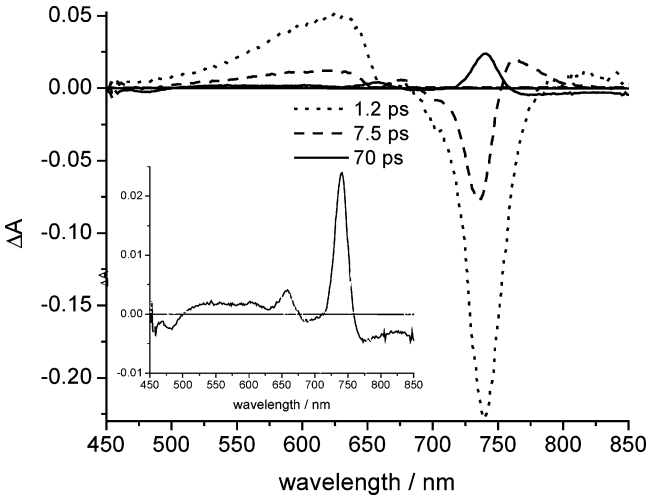

Figure 6. Three spectral cuts at 1.2 ps (dotted), 7.5 ps (dashed), and 70 ps (solid) taken from the surfaces shown in Figure 5.

shows the results of a cyclic voltammetry sequence on compound I in DCM. The first oxidation wave is at 650 mV. Similar experiments with the free base H_2Pc(BuO)$_8$ showed similar behavior. Moreover the reduction cycle showed that the singly reduced species had significant absorption to the red side of the ground state 0,0 band, as in the case of the oxidized species.

Ultrafast Transient Absorption Spectrometry. A solution of NiPc(BuO)$_8$ (ca 10 μM) in toluene was irradiated with ca. 100 fs excitation pulses at 660 or 730 nm, and the pump−probe method was employed to record optical absorption spectra at a series of delay times after the excitation pulse. The transient absorption spectra and kinetics were found to be identical irrespective of excitation wavelength. Figure 5 shows a perspective view of the first 10 ps of the dynamic surface of the A(λ,t) acquired by the spectrometer. Figure 6 shows absorption−time plots extracted from the surface at 1.0, 7.5, and 100 ps after excitation at 730 nm.

The main features of the transient spectrum at early times as seen in Figures 5 and 6 were a prompt negative absorption mirroring the ground-state spectrum (Figure 3) with extrema at 660 and 730 nm, a positive absorption from 450 to 650 nm and

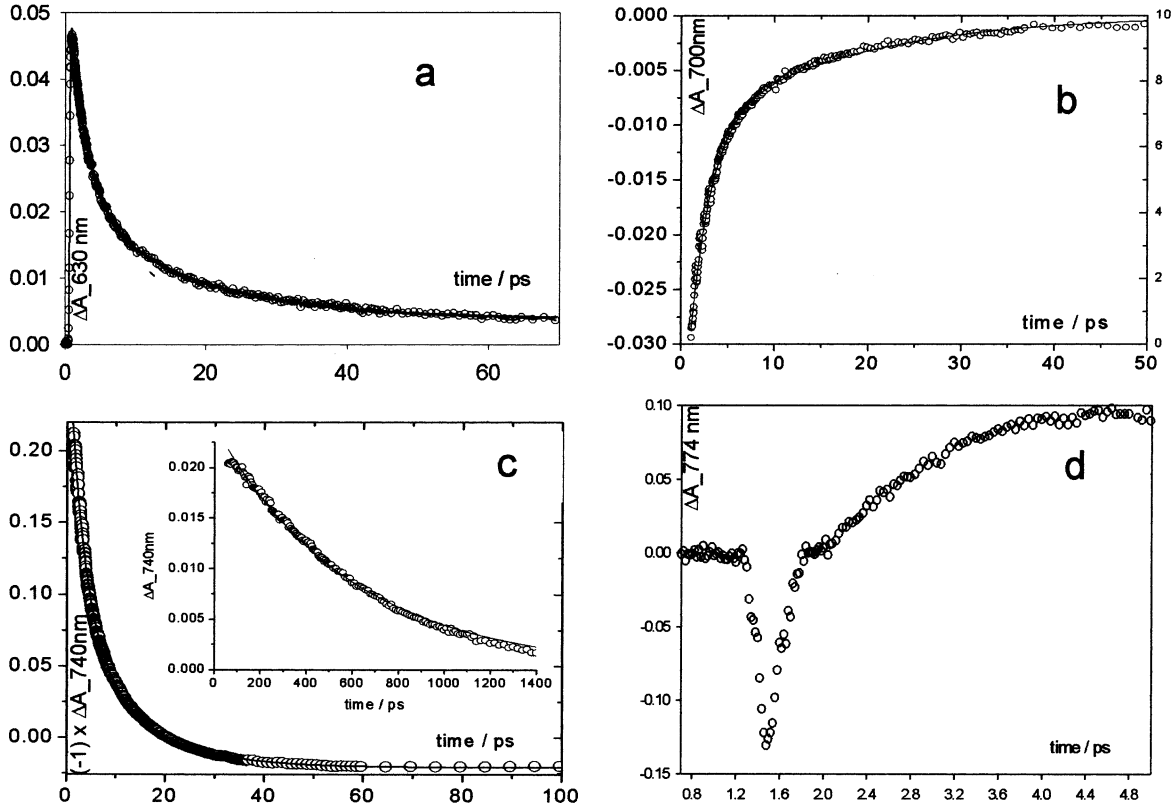

Figure 7. Representative time profile cuts at 630 nm (a), 700 nm (b), 740 nm (c and inset), and at 774 nm (d).

a positive absorption on the red side of the ground-state bleaching, that is formed with a delay. The prompt absorption changes were complete within the instrument response time (~180 fs). The decay of the positive absorption from 450 to 650 nm was best described by biexponential decay kinetics (Figure 7a) with a fast component having a lifetime of 2.3 ± 0.4 ps, and slower decay component of 15 ± 1 ps.

The negative absorption in the 650−740 nm region exhibited complex recovery kinetics. In the spectral region from 690 to 710 nm the negative absorption recovered to a zero level (Figure 7b) in a biexponential manner with lifetimes of 2.2 ± 0.2 ps and 15.2 ± 0.6 ps. These lifetimes correspond closely to those measured for the positive visible absorption (625 nm). Further to the red side (>715 nm), the negative signal recovery proceeded above the pre-pulse zero (Figure 7c) before eventually decaying back to the zero level with a lifetime of 640 ps. At 770 nm and beyond (Figure 7d), the absorbance post-pulse grew up in intensity from the zero level with a lifetime of 2.2 ps. Scrutiny of the dynamic surface in Figure 5 (first 10 ps) shows that the positive absorption band appearing at the red edge of the ground-state bleaching shows absorption maxima that shift to the blue as the amplitude increases in time. At 755 nm, the absorption band grew in with a 2.5 ps formation lifetime and decayed back to a zero baseline with a lifetime of 18.6 ± 0.3 ps. The three spectra displayed in Figure 6 summarize the results of the kinetic changes described. These, together with the kinetic profiles presented in Figure 7, clearly reveal that there are three kinetically and spectrally distinct species generated between the excitation event and the final relaxation back to the initial state.

Ground-State Molecular and Electronic Structure. The remarkable distortions from planarity of $NiPc(BuO)_8$ in its solid state structure (Figure 1) poses the question whether they are dictated by intrinsic electronic factors, such as the necessity to minimize the steric hindrance between the lone pairs of the facing oxygen atoms while preserving an efficient nickel−phthalocyanine interaction, and hence are retained in solution, or they are merely dictated by packing requirements. To answer this question that is of some relevance since we are attempting to understand the photophysics of $NiPc(BuO)_8$ in diluted solutions, we performed unconstrained geometry optimization of the model complex $NiPc(MeO)_8$ taking as starting geometry that of the crystal structure of $NiPc(BuO)_8$. The optimization converged to a minimum energy structure of D_{2d} symmetry with the carbon atoms of the methyl groups, C_{met}, coplanar with the indole rings. The same minimal energy geometry was found whether the optimization was symmetry-constrained or not. The most important geometrical parameters calculated for this structure are gathered in Table 3 and compared to the experimental values of the crystalline $NiPc(BuO)_8$.

TABLE 2: Selected Bond Distances (Å) and Angles (deg) for $NiPc(BuO)_8$

Ni(1)−N(1)	1.868(4)	N(4)−C(25)	1.362(6)
Ni(1)−N(2)	1.883(4)	N(4)−C(32)	1.373(5)
Ni(1)−N(3)	1.875(4)	N(5)−C(8)	1.325(5)
Ni(1)−N(4)	1.886(4)	N(5)−C(9)	1.321(5)
N(1)−C(1)	1.378(5)	N(6)−C(16)	1.311(6)
N(1)−C(8)	1.385(6)	N(6)−C(17)	1.322(5)
N(2)−C(9)	1.370(6)	N(7)−C(24)	1.315(6)
N(2)−C(16)	1.384(5)	N(7)−C(25)	1.325(6)
N(3)−C(17)	1.371(5)	N(8)−C(1)	1.327(6)
N(3)−C(24)	1.377(6)	N(8)−C(32)	1.311(6)
N(1)−Ni(1)−N(2)	90.1(2)	C(16)−N(6)−C(17)	120.1(4)
N(1)−Ni(1)−N(3)	173.4(2)	C(24)−N(7)−C(25)	120.0(5)
N(1)−Ni(1)−N(4)	90.3(2)	C(1)−N(8)-C(32)	120.0(4)
N(2)−Ni(1)−N(3)	90.3(2)	N(1)−C(1)-N(8)	126.5(5)
N(2)−Ni(1)−N(4)	173.3(2)	N(1)−C(8)-N(5)	126.7(4)
N(3)−Ni(1)−N(4)	90.1(2)	N(2)−C(9)-N(5)	126.3(4)
C(1)−N(1)-C(8)	106.5(4)	N(2)−C(16)-N(6)	127.1(4)
C(9)−N(2)−C(16)	107.5(4)	N(3)−C(17)-N(6)	126.0(4)
C(17)−N(3)−C(24)	106.8(4)	N(3)−C(24)-N(7)	127.2(4)
C(25)−N(4)−C(32)	107.3(4)	N(4)−C(25)-N(7)	126.6(4)
C(8)−N(5)−C(9)	120.2(4)	N(4)−C(32)−N(8)	127.2(4)

According to the data in the Table, there is a close agreement between the geometrical parameters calculated for the D_{2d}

TABLE 3: Selected Bond Lengths (Å), Bond Angles (deg), and Metrical Parameters in Crystalline NiPc(BuO)$_8$ Compared with the Corresponding Theoretical, Optimized Values of the Model NiPc(MeO)$_8$ Complex in the D_{4h} and D_{2d} conformations

	NiPc(MeO)$_8$		
	D_{4h}	D_{2d}	expt.[a]
Ni−N$_p$	1.918	1.900	1.878(4)
C$_\alpha$-N$_p$	1.384	1.382	1.376(6)
C$_\alpha$-C$_\beta$	1.454	1.453	1.455(7)
C$_\beta$-C$_\beta$	1.405	1.406	1.397(7)
C$_\alpha$-N$_b$	1.317	1.319	1.320(6)
C$_o$-O	1.364	1.363	1.361(6)
∠C$_\alpha$N$_p$C$_\alpha$	107.1	107.5	107.0(4)
∠C$_\alpha$N$_b$C$_\alpha$	121.8	121.2	120.1(4)
O···O	3.500	3.793	3.91(2)
|ΔN$_p$|	0.0	0.111	0.109(4)
|ΔN$_b$|	0.0	0.0	0.056(4)
|ΔC$_\alpha$|	0.0	0.243	0.268(5)
|ΔC$_\beta$|	0.0	0.597	0.670(5)
|ΔC$_o$|	0.0	0.917	1.015(6)
|ΔC$_m$|	0.0	1.232	1.319(6)
|ΔO|	0.0	0.919	1.043(4)
∠(C$_\alpha$N$_p$N$_p$C$_\alpha$)$_{op}$	0.0	0.0	2.9(6)
∠(C$_\alpha$N$_p$N$_p$C$_\alpha$)$_{ad}$	0.0	12.5	16.2(4)

[a] X-ray data, this work.

conformer and the experimental averaged values. Thus, apart from the modest ruffling of the phthalocyanine skeleton and the random displacements of the C$_{but}$ atoms from the indole rings (most likely related to packing requirements) the salient features of the solid-state structure of NiPc(BuO)$_8$ are substantially preserved in the D_{2d} geometry of the model system.

We have also tried to determine the motion from one saddle structure to the opposite saddled structure (with the other indole rings up and down) through a planar D_{4h} structure (the most commonly adopted by monomeric metallophthalocyanines). Surprisingly, we found that the D_{4h} is only ca. 1 kcal/mol less stable than the D_{2d} structure. Table 3 lists the relevant geometrical parameters calculated for this geometry, whence it is apparent that the most conspicuous effects of flattening the molecule consist of lengthening the Ni−N$_p$ distance by 0.018 Å, and a considerable shortening (0.29 Å) of the distance between facing oxygen atoms. The increased steric repulsion between the facing oxygen lone pairs and the less efficient metal−macrocycle interactions would lead to the expectation that the planar structure should be far less stable than the saddled one. That this is not the case suggests that the energy cost of the saddling (mostly ring strain) almost cancels the energy gain coming from the relief of steric repulsion between the facing oxygen lone pairs and the improved metal−macrocycle interaction.

We have verified by explicit frequency calculations that the saddled structures are true minima (all positive frequencies) and that the D_{4h} structure is indeed a maximum, with one imaginary frequency corresponding to the saddling motion (of b_{2u} symmetry). Given the inherent limitation of these calculations (basis set choice, functional used, numerical accuracy, neglect of solvation effects, no information on entropic effects, including those from solvent environment, truncation of the alkyl chains) we cannot be specific about the precise height of the barrier and the frequency of the flapping motion. The calculations, however, clearly indicate that while in the solid state the molecule is "frozen" in the saddled structure, in solution it can flap from one saddled conformation through the planar "maximum" to the opposite saddled structure. Therefore, for completeness, it is deemed necessary to consider also the D_{4h} structure.

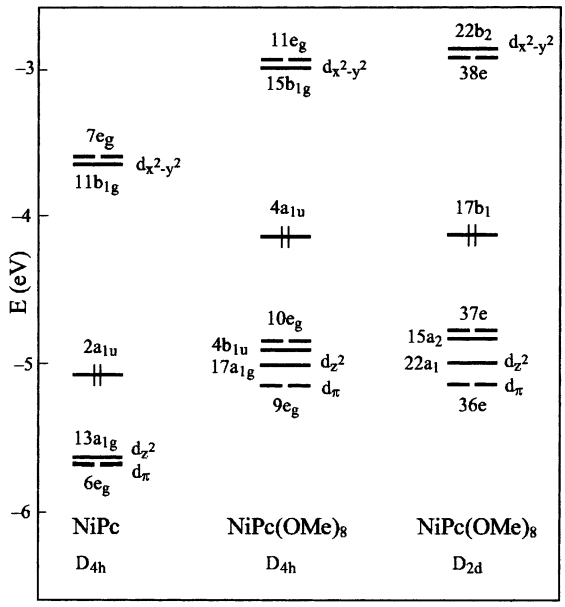

Figure 8. Energy level scheme for NiPc and NiPc(MeO)$_8$.

The highest occupied and the lowest unoccupied ground-state one electron levels calculated for NiPc(MeO)$_8$ in the D_{2d}-saddled and D_{4h}-planar conformations are shown in Figure 8 where, for comparison purpose, the ground-state one-electron levels of NiPc are also shown. In our choice of the axes, the *z* axis is perpendicular to the plane of the *meso*-nitrogen atoms, the *x* and *y* axes bisect the indole rings in the planar D_{4h} structure and point to the *meso*-nitrogen atoms in the saddled D_{2d} structure.

Since an extensive discussion of the electronic structure of NiPc has been published,[20−22] we recall here only the most salient features.

Among the NiPc levels in Figure 8, one may recognize, apart from the π G-2a$_{1u}$ and the π^* G-7e$_g$ (G = Gouterman) orbitals, the metal 3d orbitals. In the virtual spectrum, there is the 3d$_{x^2-y^2}$ (11b$_{1g}$), which is pushed up by antibonding with the N$_p$ lone pairs. Actually, the 11b$_{1g}$ is composed of 3d$_{x^2-y^2}$ and N$_p$ lone pairs in almost equal amount. The highest occupied 3d levels are the 3d$_{z^2}$ (13a$_{1g}$), which is an almost pure metal orbital, and the 3d$_\pi$ (6e$_g$). The 6e$_g$ is heavily (41%) mixed with the N$_p$ based π orbitals of the phthalocyanine ring. Its bonding counterpart is the 4e$_g$ orbital, lying 1.3 eV below. The level pattern of the NiPc(MeO)$_8$ conformers shows that introducing methoxy groups into the Pc destabilizes all of the levels, but preferentially the G-2a$_{1u}$ (4a$_{1u}$ and 17b$_1$ in the D_{4h} and D_{2d} conformers, respectively). The preferential destabilization of the HOMO fits in with the antibonding, visible in the plot of this orbital displayed in Figure 9, between the Pc-a$_{1u}$, which has large amplitude on the ortho-carbons of the benzo rings, and the oxygen lone pairs of the methoxy groups whose contribution to this orbital amounts to ∼15%.

Owing to the upshift of the HOMO, the energy gap between the occupied G-a$_{1u}$ and the unoccupied G-e$_g$* is reduced in NiPc-(MeO)$_8$ with respect to NiPc.

The 2b$_{1u}$ is another π orbital of the macrocycle which is strongly destabilized by interaction with the oxygen lone pairs. In NiPc(MeO)$_8$, the 2b$_{1u}$ derived orbital, the 4b$_{1u}$ in the planar and the 15a$_2$ in the saddled conformer, is upshifted with respect to the NiPc-2b$_{1u}$ by 1.8 eV (in NiPc the 2b$_{1u}$ is too low in energy

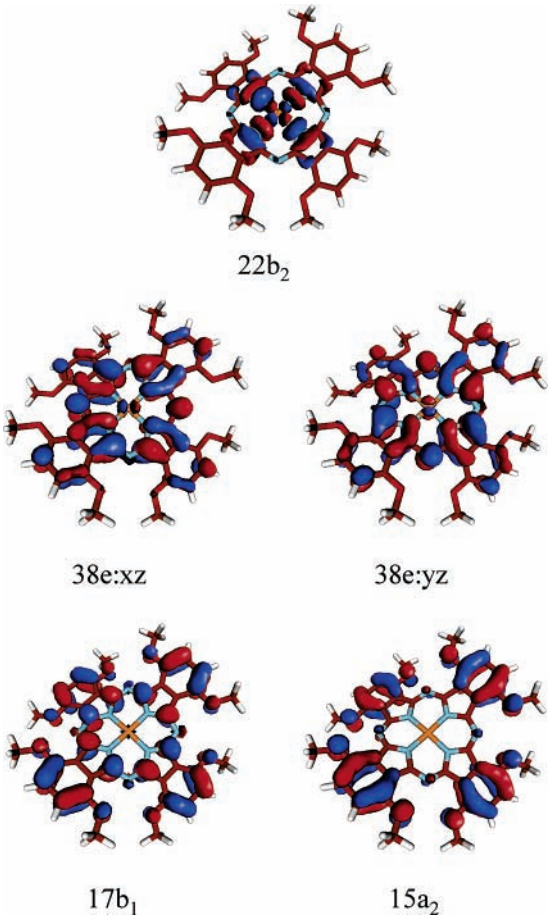

Figure 9. Contour plots of the $17b_1$ (HOMO), $15a_2$, 38e (LUMOs), and $22b_2$ orbitals of NiPc(MeO)$_8$ in the D_{2d} geometry.

to enter the diagram of Figure 8). Because of its large amplitude (~50%) on the carbon atoms at the ortho positions of the benzo rings, the $2b_{1u}$ heavily (30%) mixes in antibonding fashion with the oxygen lone pairs, as inferred by the plot of the $15a_2$ displayed in Figure 9.

As for the metal states, the introduction of the methoxy groups does not modify the salient features of the nickel−phthalocyanine interactions, although their energy and composition sense to some extent the change in the relative energy of the macrocycle and the metal. For instance, going from NiPc to NiPc(MeO)$_8$, the $3d_\pi$ contribution to the π bonding/antibonding pair is reversed. Most of the $3d_\pi$ character is found in the $9e_g$ (36e), its antibonding counterpart, the $10e_g$ (37e) having only a 20% of Ni-$3d_\pi$ character.

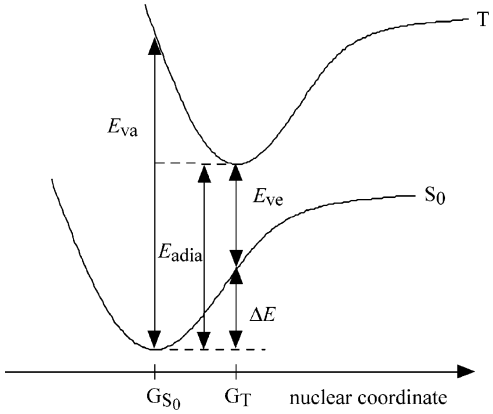

Figure 10. Schematic definition of the computed excitation energies. ΔE is calculated as $E(S_0,G_T) - E(S_0,G_{S0})$.

When comparing the level scheme of the two NiPc(MeO)$_8$ conformers, it is apparent that the most conspicuous effect of the $D_{4h} \rightarrow D_{2d}$ geometry change is the upshift of the Ni-$d_{x^2-y^2}$ level ($22b_2$), which ends up slightly above the G-e_g*(38e). The destabilization of the $22b_2$ ($d_{x^2-y^2}$), which is a strongly σ antibonding Ni−N_p orbital (see the plot in Figure 9), is in line with the shortening of the Ni−N_p distance on going from the planar to the saddled conformation (see Table 3). As will be seen later, the relative position of the unoccupied $d_{x^2-y^2}$ metal level with respect to the occupied metal levels, notably the d_{z^2} and the ligand G-a_{1u} are crucial for the photophysical behavior of NiPc(BuO)$_8$.

Excited States and Ground-State Absorption Spectrum. TDDFT calculations were employed to examine the lowest triplet and singlet excited states of the two NiPc(MeO)$_8$ conformers. The vertical absorption energies (E_{va}) calculated for the whole set of triplet and singlet states up to 1.9 eV are gathered in Table 4 together with the adiabatic energies (E_{adia}) calculated for selected excited states.

The vertical absorption energies E_{va} have been evaluated at the ground-state optimized geometry. The adiabatic energies have been obtained according to the expression

$$E_{adia} = E_{ve} + \Delta E$$

E_{ve} is the vertical emission energy, which is calculated at the TDDFT level using the relaxed excited-state geometry. The ΔE term accounts for the change in energy of the ground state upon deformation to the relaxed geometry of the excited state (for a schematic definition of the calculated energies see Figure 10).

In Table 5, the vertical absorption energies (E_{va}) and oscillator strengths calculated for the optically allowed excited states

TABLE 4: Excitation Energies (eV) Computed for the Low-Lying Excited States of NiPc(MeO)$_8$

D_{2d}					D_{4h}				
state	composition (%)	character	E_{va}	E_{adia}	state	composition (%)	character	E_{va}	E_{adia}
2^1A_2	100 ($37e \rightarrow 38e$)	π,π^*	1.90		1^1A_{2g}	100 ($10e_g \rightarrow 11e_g$)	π,π^*	1.90	
2^3A_2	100 ($37e \rightarrow 38e$)	π,π^*	1.88		1^1A_{1u}	100 ($4b_{1u} \rightarrow 15b_{1g}$)	LMCT	1.90	
1^3B_1	100 ($37e \rightarrow 38e$)	π,π^*	1.86		1^3A_{1u}	100 ($4b_{1u} \rightarrow 15b_{1g}$)	LMCT	1.90	
2^3B_2	100 ($37e \rightarrow 38e$)	π,π^*	1.83		1^3A_{2g}	100 ($10e_g \rightarrow 11e_g$)	π,π^*	1.88	
2^3E	80 ($37e \rightarrow 22b_2$) 20 ($36e \rightarrow 22b_2$)	LMCT/d_π,$d_{x^2-y^2}$	1.83		1^3B_{2g}	100 ($10e_g \rightarrow 11e_g$)	π,π^*	1.86	
1^3A_1	100 ($37e \rightarrow 38e$)	π,π^*	1.80		1^3A_{1g}	100 ($10e_g \rightarrow 11e_g$)	π,π^*	1.82	
1^3B_2	98 ($22a_1 \rightarrow 22b_2$)	d_{z^2},$d_{x^2-y^2}$	1.69	1.39	1^3E_g	77 ($10e_g \rightarrow 15b_{1g}$) 22 ($9e_g \rightarrow 15b_{1g}$)	LMCT/d_π,$d_{x^2-y^2}$	1.66	
1^1E	91 ($17b_1 \rightarrow 38e$)	π,π^*	1.60		1^1E_u	90 ($4a_{1u} \rightarrow 11e_g$)	π,π^*	1.60	
					1^3B_{1g}	100 ($17a_{1g} \rightarrow 15b_{1g}$)	d_{z^2},$d_{x^2-y^2}$	1.58	1.08
1^1A_2	100 ($17b_1 \rightarrow 22b_2$)	LMCT	1.28	1.15[a]	1^1B_{1u}	100 ($4a_{1u} \rightarrow 15b_{1g}$)	LMCT	1.19	0.88[a]
1^3A_2	100 ($17b_1 \rightarrow 22b_2$)	LMCT	1.27	1.13	1^3B_{1u}	100 ($4a_{1u} \rightarrow 15b_{1g}$)	LMCT	1.17	0.87
1^3E	100 ($17b_1 \rightarrow 38e$)	π,π^*	1.15	1.09 (1^3B_2)	1^3E_u	90 ($4a_{1u} \rightarrow 11e_g$)	π,π^*	1.16	1.04 (1^3B_{3u})

[a] Computed at the optimized geometry of the corresponding triplet.

TABLE 5: Vertical Excitation Energies and Oscillator Strengths (f) Computed for the Optically Allowed Excited States of the D_{4h} and D_{2d} NiPc(MeO)$_8$ Conformers Contributing to the Q-Band Region Are Compared to the Experimental Data

D_{4h}				D_{2d}				exp.[a]
state	composition (%)	E_{va} (eV/nm)	f	state	composition (%)	E_{va} (eV/nm)	f	E (eV/nm)
1^1E_u	90 ($4a_{1u} \rightarrow 11e_g$)	1.60/775	0.492	1^1E	91 ($17b_1 \rightarrow 38e$)	1.60/775	0.513	1.69/734 Q
2^1E_u	93 ($4b_{1u} \rightarrow 11e_g$)	2.07/599	0.391	1^1B_2	92 ($37e \rightarrow 38e$)	2.02/614	0.012	sh
				2^1E	92 ($15a_2 \rightarrow 38e$)	2.07/599	0.357	

[a] Toluene solution spectrum of NiPc(BuO)$_8$, this work.

contributing to the Q-band region are compared to the experimental data. Tables 4 and 5 also include the compositions of the BP/ALDA solution vectors in terms of the major one-electron MO transitions.

We discuss first the TDDFT results for the optically allowed excited states in order to provide an assignment of the ground-state absorption spectrum of NiPc(BuO)$_8$ in the Q-band region. On the basis of the computed energies and oscillator strengths, the intense Q(0,0) band with maximum at 734 nm is assigned to the lowest optically allowed excited state, the 1^1E, computed for the model system, NiPc(MeO)$_8$, at 1.60 eV (775 nm), in satisfactory agreement with the experiment. As inferred from the composition of the excited states, the Q state is an almost pure G-$a_{1u} \rightarrow$ G-e_g* ($17b_1 \rightarrow 38e$) state. The large destabilization of the $17b_1$ induced by the methoxy groups causes the G-a_{1u}/G-e_g* energy gap to be in NiPc(MeO)$_8$ sensibly narrower than in the parent NiPc, which fits in with the Q-band being in NiPc(BuO)$_8$ red shifted relative to NiPc by $\sim$70 nm.

In the energy regime of the Q-band, we predict a second intense excited state, the 3^1E. This state, computed at 2.07 eV (599 nm), accounts for the broad absorption appearing in the spectrum of NiPc(BuO)$_8$ to the blue of the Q(1,0) band. This assignment is fully consistent with this feature being related to the presence of the butoxy groups at the periphery of the phthalocyanine ring. Indeed, the 3^1E is largely derived from promotion of one electron from the $15a_2$, a π orbital of the macrocycle which has large amplitude on the oxygen lone pairs, to the G-e_g* derived 38e. A third, very weak, excited state, the 1^1B_2, is predicted in the Q-band region. This state, computed at 2.02 eV (614 nm), contributes to the broadening of the region to the blue of the Q(1,0) band.

According to the TDDFT results in Table 5, the electronic transitions computed for the D_{4h} conformer are essentially identical in energy, intensity, and character to those computed for the D_{2d} conformer. This indicates that the flapping motion of the molecule from one saddled conformation through the planar "maximum" to the opposite saddled structure, if any, would not be detectable in the optical spectrum.

Besides the optically allowed excited states above-discussed, a manifold of triplet and singlet symmetry forbidden excited states are calculated in the energy regime of the Q-band (see Table 4). These "dark" states are likely to play a role in the observed radiationless decay of the primarily excited S_1 (π,π*) state and thus deserve detailed discussion. The TDDFT results for the D_{2d} structure indicate that three "dark" states lie vertically below the S_1 (π,π*) state. They are the 1^1A_2, 1^3A_2, and 1^3E, which appear vertically at 1.28, 1.27, and 1.15 eV, respectively. These are the most plausible candidates as deactivation channels for the S_1 (π,π*).

According to the composition of the BP/ALDA solution vectors in Table 4, the 1^3E is the normally emissive $^3(\pi,\pi^*)$ state, whereas the 1^1A_2 and 1^3A_2 are pure $17b_1 \rightarrow 22b_2$ LMCT states.[41-46] The $^1A_2/^3A_2$ splitting is very small, on account of the delocalized character of the MOs involved in the one-electron transition, the $17b_1$ being a π orbital of the macrocycle and the $22b_2$ a nearly 50/50 mixture of Ni-$3d_{x^2-y^2}$ and N_p lone pairs.

TABLE 6: Optimized Geometrical Parameters (Å and deg) for NiPc(MeO)$_8$ in the D_{2d} Ground State ($^1A_1$) and in the Lowest Triplet Excited States

	$^1A_1$	$^3B_2$[a]	$^3A_2$[a]	$^3B_2$
Ni$-N_p$	1.900	1.972	1.957	1.900/1.900
C_α-N_p	1.382	1.376	1.374	1.386/1.384
C_α-C_β	1.453	1.460	1.465	1.464/1.440
C_β-C_β	1.406	1.413	1.410	1.403/1.416
C_α-N_b	1.319	1.328	1.327	1.308/1.338
C_o-O	1.363	1.363	1.362	1.360/1.361
$\angle C_\alpha N_p C_\alpha$	107.5	109.5	108.8	107.8/107.6
$\angle C_\alpha N_b C_\alpha$	121.2	123.6	123.1	120.5
O$\cdots$O	3.793	3.844	3.917	3.916
$\lvert\Delta N_p\rvert$	0.111	0.069	0.045	0.093/0.114
$\lvert\Delta N_b\rvert$	0.0	0.0	0.0	0.003
$\lvert\Delta C_\alpha\rvert$	0.243	0.205	0.225	0.257/0.294
$\lvert\Delta C_\beta\rvert$	0.597	0.552	0.641	0.684/0.725
$\lvert\Delta C_o\rvert$	0.917	0.901	1.024	1.069/1.107
$\lvert\Delta C_m\rvert$	1.232	1.242	1.401	1.452/1.481
$\lvert\Delta O\rvert$	0.919	0.908	1.028	1.068/1.109
$\angle(C_\alpha N_p N_p C_\alpha)_{op}$	0.0	0.0	0.0	0.0
$\angle(C_\alpha N_p N_p C_\alpha)_{ad}$	12.5	12.6	15.9	15.9

[a] The geometry optimization was performed under D_{2d} symmetry constraint.

As inferred from the data in Table 4, the adiabatic energies of the 1^3A_2 and 1^1A_2 (the E_{adia} value of the 1^1A_2 was obtained using the relaxed geometry of the corresponding triplet, so it can be considered as upper limit to the actual value) are significantly decreased by 0.13 and 0.14 eV relative to the value of the corresponding vertical absorption energies. This fits in with the relaxed geometry of the 1^3A_2 showing significant changes with respect to the ground-state geometry, as can be seen in Table 6 which collects the optimized geometries of the lowest-lying triplet excited states and, for the sake of comparison, the geometry of the ground state. The relaxed geometry of the 1^3A_2 is characterized by a considerable lengthening of the Ni$-N_p$ distance and a sizable expansion of the macrocycle core. These geometrical changes are directly related to occupation of the $22b_2$, a strongly σ antibonding Ni$-N_p$ orbital (see plot in Figure 9).

As for the 1^3E (π,π*) excited state, it is doubly degenerate and is expected to Jahn$-$Teller (J$-$T) distort into a D_2 or C_{2v} structure along the b_1 or b_2 active modes, respectively. To estimate the vibrational relaxation shift of the 1^3E (π,π*) $\rightarrow$ $1^1A_1(S_o)$ transition we performed geometry optimization of the 1^3E (π,π*) state. It turned out that the D_{2d} symmetry is no longer stable in this state and it is lowered to C_{2v}. The resulting 1^3B_2 electronic state, which originates from the HOMO-$32a_2$ ($17b_1$ in the D_{2d} symmetry) to the $38b_1$ (the xz component of the D_{2d} 38e) one-electron excitation, fails to show significant geometrical relaxation, as can be inferred from the structural parameters gathered in Table 6. In line with the minor conformational relaxation, the adiabatic $S_o \rightarrow T_1$ ($^3B_2$) transition energy is only 0.06 eV lower than the vertical absorption energy.

An important point to arise from the above TDDFT results is that in NiPc(BuO)$_8$ the ^{1,3}LMCT states involving excitation out of the G-a$_{1u}$ into the Ni-d$_{x^2-y^2}$ MO may provide effective routes for deactivation not only for the $^1(\pi,\pi^*)$ (the $^{1,3}A_2$ LMCT states are found to lie vertically ~0.3 eV below the normally fluorescent S_1 state) but also for the normally phosphorescent $^3(\pi,\pi^*)$. Indeed, the minima of the $^{1,3}A_2$ LMCT and $^3(\pi,\pi^*)$ relaxed energy hypersurfaces are found to lie at nearly the same energy.

Coming now to the excited states lying vertically above the 1^1E (π,π^*) state, most of them are of (π,π^*) character and are not expected to undergo significant conformational relaxation. Therefore, it is unlikely their relaxed energy surfaces would cross the S_1 (π,π^*) surface. On the contrary, this may happen for the 1^3B_2(d,d) and 2^3E(LMCT/d,d) excited states.

The 1^3B_2 is mainly described by the $22a_1 \rightarrow 22b_2$ ($d_{z^2} \rightarrow d_{x^2-y^2}$) transition. Its corresponding singlet, the 4^1B_2, is calculated at a much higher energy (2.92 eV). Such a large singlet/triplet splitting fits in with the high localization of the unpaired electrons on the metal center. Similar to the 1^3A_2 LMCT state discussed above, this state undergoes large conformational relaxation. From Table 6 where the 1^3B_2 relaxed geometry is reported, the lengthening of the Ni−N$_p$ distance and the expansion of the macrocycle core following population of the strongly Ni−N$_p$ antibonding $22b_2$ MO are even larger than in the 1^3A_2. In line with the remarkable conformational relaxation, the adiabatic excitation energy of the 1^3B_2 is predicted to be 0.3 eV lower than the vertical absorption energy. The geometrical relaxation of the 1^3B_2 suggests that its relaxed potential energy hypersurface crosses the 1^1E (π,π^*) surface thereby opening a route for an efficient ISC mechanism.

Besides the ^{3}(d,d) just discussed, another excited state may become involved in the decay of the primarily excited S_1 (π,π^*) state, the 2^3E. This state is predicted to lie vertically 0.24 eV above the 1^1E (π,π^*). However, similar to the $^3(d_{z^2},d_{x^2-y^2})$ and 1^3A_2(LMCT), it is expected to undergo large geometrical relaxation. The 2^3E excited state is indeed described by one-electron transitions, the $37e \rightarrow 22b_2$ ($\pi \rightarrow d_{x^2-y^2}$), and the $36e \rightarrow 22b_2$ ($d_\pi \rightarrow d_{x^2-y^2}$), which involve population of the strongly Ni−N$_p$ antibonding $22b_2$ MO.

The TDDFT results for the flat geometry (D_{4h} in the ground state) proved to be similar to those for the D_{2d} geometry. The major effect of flattening the molecule is to lower the $^3(d_{z^2},d_{x^2-y^2})$ and ^{1,3}LMCT excited states, which is a consequence of the downward shift of the Ni $d_{x^2-y^2}$ MO upon lengthening of the Ni−N$_p$ bond distance (cf Table 3 and Figure 8). Of the states that are the most plausible candidates for radiationless deactivation of the initially populated $S_1(\pi,\pi^*)$ state, the $^3(d_{z^2},d_{x^2-y^2})$ (1^3B_{1g}) is found to lie vertically at nearly the same energy as the $^1(\pi,\pi^*)$ (1^1E_u). So is the ^{1,3}LMCT ($1^{1,3}B_{1u}$) pair with respect to the $^3(\pi,\pi^*)$ (1^3E_u). The 1^3B_{1g} and $1^{1,3}B_{1u}$ states, similar to the corresponding D_{2d} 1^3B_2 and $1^{1,3}A_2$, undergo large conformational relaxation. The geometrical changes (not reported here), which are mainly related to occupation of the strongly σ antibonding Ni−N$_p$ orbital, the $15b_{1g}$, consist of a considerable lengthening of the Ni−N$_p$ distance and a sizable expansion of the macrocycle core, both effects being largest in the 1^3B_{1g} excited state. On account of the remarkable conformational relaxation, the adiabatic excitation energy of the 1^3B_{1g} is decreased by 0.5 eV with respect to the value of the corresponding vertical absorption energy. This implies that the minimum of the relaxed energy hypersurfaces of the $^3(d_{z^2},d_{x^2-y^2})$ will be located well below the minimum of the 1^1E_u (π,π^*) hypersurface.

The lowest excited state, the potentially phosphorescent 1^3E_u (π,π^*), relaxes to a rectangular D_{2h} structure, due to J−T instability. The geometrical relaxation is not very large, thus the vertical emission energy of the resulting $^3B_{3u}$ electronic state, originating from the HOMO-8a$_u$ ($4a_{1u}$ in the D_{4h} symmetry) to the $11b_{3g}$ (the *yz* component of the D_{4h} $11e_g$) one-electron excitation, is only 0.12 eV lower than the vertical absorption energy calculated for the unrelaxed 1^3E_u (π,π^*). Therefore, the minimum of the relaxed energy hypersurface of the 1^3B_{3u} (π,π^*) is somewhat higher than the minima of the relaxed energy hypersurfaces of the ^{1,3}LMCT states which, on the contrary, experience a larger energy relaxation (~0.3 eV).

In summary, the $^3(d_{z^2},d_{x^2-y^2})$ and the ^{1,3}LMCT states appear to be the main actors in the radiationless decay of the primarily excited S_1 (π,π^*) state regardless the conformation assumed by the molecule.

Summation of the Theoretical and Experimental Results. In the following section, the experimental results of the ultrafast studies are examined in the light of the insights that have been gained from the theoretical efforts. To simplify the arguments, we concentrate on the theoretical results obtained for the stable D_{2d} structure of the model complex, NiPc(MeO)$_8$, and later point out the effects of the flapping motion through a planar D_{4h} structure.

For NiPc(BuO)$_8$ in toluene, the spectral data presented in Figures 5 and 6 indicate that photoexcitation at 660 or 730 nm (both wavelengths pump the $S_0 \rightarrow S_1$ electronic transition) generated an absorbing entity in the 450 nm to 650 nm region that is fully formed during the instrument response function (ca 180 fs), this is also true for the negative absorbing component at 730 nm. However, in the spectral region to the red side of the ground-state bleach (>770 nm), no absorption was present at the earliest times (Figure 6, dotted), but a positive signal grows up over the succeeding few ps (Figure 6, dashed). The 1 ps (dotted) spectrum shown in Figure 6 has a broad signature in the 450 nm upward region, superimposed on which is the inverse of the ground-state UV−vis spectrum as displayed in Figure 3. Thus, according to expectations, the excitation pulse removes ground-state molecules as it generates the first observed transient (FOT). Since the excitation induces the $S_0 \rightarrow S_1$ transition, it is conceivable that the 1 ps spectrum (dots) in Figure 6 is that of the ^1Q state (via the $S_1 \rightarrow S_n$ transition) of NiPc(BuO)$_8$, or it may be that of some species generated from ^1Q at times shorter than can be resolved here. The $S_1 \rightarrow S_n$ transition is of π-character, being localized within the orbitals of the phthalocyanine ligand. However, TDDFT results indicate that at least five states, viz. the 2^3E, 1^3B_2, 1^1A_2, 1^3A_2, and 1^3E, may provide effective routes for the radiationless decay of the primarily excited $S_1(\pi,\pi^*)$ state. Thus the FOT could be a state with some amount of metal character, e.g. the 1^3B_2 $^3(d_{z^2},d_{x^2-y^2})$ or the $1^{1,3}A_2$ LMCT. If the FOT were the 1^3B_2 its difference spectrum would be expected to resemble the simulated spectrum shown as the full line spectrum in Figure 11. This simulation was made by removing a fraction of the absorbance causing the dotted spectrum and adding an equal amount of that caused by the dot−dash one. These spectral entities have the same extinction coefficients within the Lorentzian envelopes and have peak wavelengths shifted by 20 nm.

The conversion of the ^1Q state into the 1^3B_2 generates a version of the complex that has a ground state π-system with a metal center in a nonground-state electronic configuration. Since the absorption spectrum in the Q-band region of the metallophthalocyanine is dominated by the $\pi \rightarrow \pi^*$ transition, and this originates from a ground state electronic configuration in the

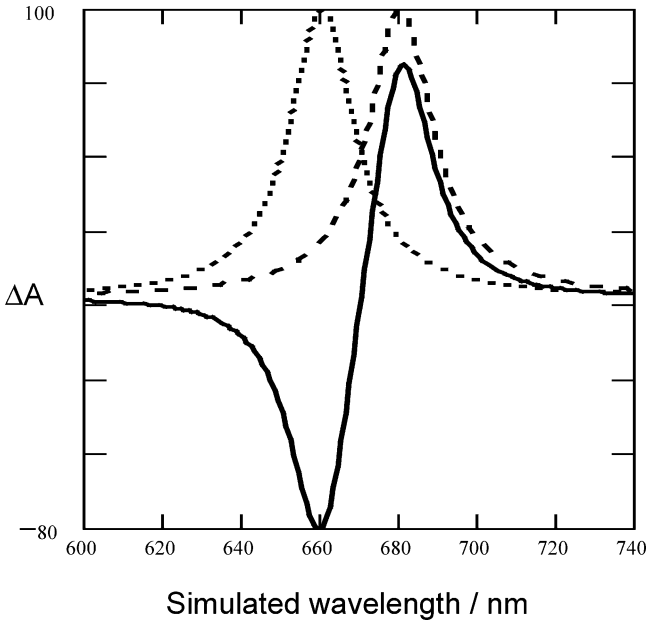

Figure 11. Simulation of the difference absorption spectrum of a d,d electronic state (see text).

ligand, modified by a nonground state d-electron configuration, the true absorption spectrum of the state should closely resemble that of the ground state of the complex with a small spectral shift due to the unusual d-electron configuration, as simulated in Figure 11. Spectral profiles such as this have been reported for Ni(II) porphyrin excited states where the $d_{z^2},d_{x^2-y^2}$ character was confirmed.[10−19] The difference spectrum of the FOT derived from NiPc(BuO)$_8$ (Figure 6, dotted) bears no resemblance to the simulated one and so the putative assignment to the 1^3B_2 is discarded. Thus, we are left with the possibility that the FOT is either the π-localized S_1 state or a state with charge-transfer character (LMCT). The optical absorption spectra for such CT states would be expected to show similarities to those of the one electron oxidized forms of the π-system. However, the spectro-electrochemical data presented in Figure 4 show significant absorbance to the red side of the ground-state Q-band, whereas the 1 ps spectrum shown in Figure 6 has no absorbance at the red side of the ground-state region. These arguments lead to the conclusion that the post-pulse spectrum is due to the ^{1}Q state formed directly from photon absorption. The decay of this entity (at 625 nm) was nonexponential but could be adequately fitted with a pair of exponentials. The major, faster component had a lifetime of 2.6 ± 0.3 ps; the weak, slower component had a lifetime of 15.1 ± 4 ps.

Having argued that the 1 ps spectrum is that of the S_1 (π,π^*) state generated directly by photon absorption, it is now necessary to assign the later transient spectra in Figure 6 (dashed and full lines). At 770 nm and beyond (Figure 7d), a positive absorption is seen to grow in from zero with a growth lifetime of 2.1 ps and having a subsequent decay with a 21 ps lifetime. Interestingly the peak wavelength of this entity became increasingly blue-shifted as time elapsed (Figure 5, first 10 ps). Similar behavior to this blue-shifting absorption peak has been observed for other phthalocyanines earlier in these laboratories when it was attributed to the cooling of a vibrationally hot daughter state with d-character.[25] At or about 8 ps, post excitation the blue shift is complete and at that point the difference spectrum is as the dashed line in Figure 6. Now the negative absorption minimum at 730 nm with the positive absorption maximum at 755 nm show the typical negative and positive lobe pattern represented by Figure 11, the implication being that the product at 8 ps is a state in which the π-system of the ligand has a ground state electronic configuration and the excitation is resident on the metal, viz. a (d,d) state. According to TDDFT calculations, this (d,d) state can only be the $^3(d_{z^2},d_{x^2-y^2})$ (1^3B_2).

That the positive and negative lobes in Figure 6 (dashed) are not equal (as in Figure 11) indicates that the stoichiometry of the conversion is not 1:1 in terms of absorbance change, either due to differences in extinction coefficient or because the (d,d) state precursor (the FOT) is being depleted through competing routes that lead elsewhere (see below).

The negative absorption centered at 740 nm that was formed within the rise time of the instrument, decayed in a biexponential manner to a nonzero baseline (Figure 7b). Lifetimes of 2.1 ± 0.3 and 22.0 ± 3 ps were extracted. The faster component has a lifetime that is close to that of the early component of the decay of the S_1 state (2.6±0.3 ps) and the first thought is that it represents a rapid radiationless conversion of S_1 to S_0. However, this transition is $\pi^* \rightarrow \pi$ in nature and such transitions in metallophthalocyanines with p-block metal centers are known to occur with lifetimes in the nanosecond regime.[26] It is more likely that this fast component of the negative signal recovery is actually the growth phase of an entity that has a positive absorption underlying that of the ground state of the complex. Such an entity is the (d,d) state represented by the 8 ps spectrum (dashed) in Figure 6.

The conclusion that the S_1 (π,π^*) state (dotted spectrum in Figure 6) converts into the $^3(d_{z^2},d_{x^2-y^2})$, 1^3B_2, with a lifetime of ca. 2 ps requires an intersystem crossing process to occur, which might a priori be thought to be inconsistent with such a short lifetime. However, according to the TDDFT calculations, the relaxed potential energy hypersurface of the $^3(d_{z^2},d_{x^2-y^2})$ is likely to cross the 1^1E (π,π^*) surface opening a route for an efficient ISC mechanism. The narrowing of the optical absorption spectrum at the red side of the ground state bleaching absorption (Figure 5) over the first 8 ps suggests that the produced (d,d) state is vibrationally hot and is capable of losing some energy to achieve its relaxed structure. The dashed spectrum shown in Figure 6 is that of the vibrationally cold (d,d) state. This state converts to a daughter state (Figure 6, full line) with a lifetime of ca. 20 ps. The difference spectrum is reminiscent of the absolute spectrum of the ground state, having a major peak at 740 nm and a minor one at 660 nm with underlying ground-state bleaching. According to the TDDFT calculations the decay product of the (d,d) state might be one of the two LMCT states, one triplet and one singlet, or the $^3(\pi,\pi^*)$ state, all lying in the S_1-S_0 gap. However, the spectral signature (Figure 6, full) bears no resemblance to that of the $^3(\pi,\pi^*)$ spectra of similar metallophthalocyanines, which typically show broad featureless absorptions with maxima near 600 nm.[26] Therefore, the full line spectrum (Figure 6) arises from one of the near degenerate LMCT states, probably the triplet sub-state, since the precursor has triplet multiplicity. An MO analysis of the ^{3}LMCT state reveals that the π/π^* energy gap increases relative to the ground state, so the ^{3}LMCT is expected to have a visible absorption spectrum similar to, but blue shifted in wavelength from, the ground state spectrum. This fits in with the full line spectrum of Figure 6 resembling the difference spectrum between two metallophthalocyanines with only a very small spectral shift to the blue. It is not inconceivable that the 1^3E (π,π^*) is, in fact, populated through the decay of the ^{3}(d,d) state, but if so the only nonradiative decay route for this state is to the LMCT state, so the net result would be the same as if the 1^3E state did not intervene. Finally, the LMCT state converts to the ground-state

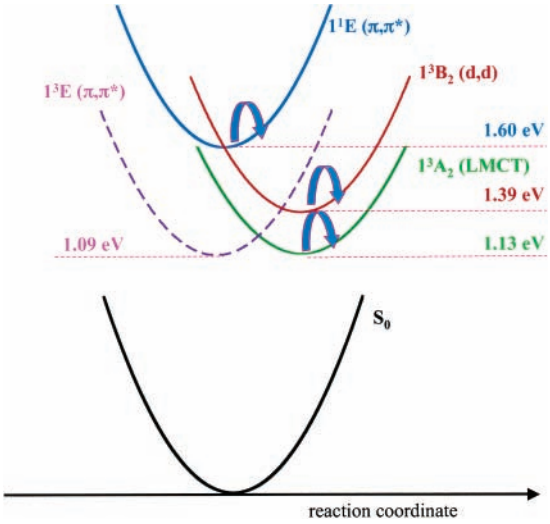

Figure 12. Schematic diagram illustrating the key photoprocesses for the photoexcited NiPc(BuO)$_8$.

surface with a lifetime of 640 ps. In sum, the Q state (S_1) of NiPc(BuO)$_8$ in toluene, generated by photoexcitation in the Q-band, deactivates in a cascade of events, populating in turn the 1^3B_2 (d,d) and the 1^3A_2 LMCT states, before finally regaining the ground state surface. The just described sequence of events is represented schematically in Figure 12, which has been constructed using the data in Table 4.

As a final note in this attempt to assign spectral signatures to states, the (d,d) state decayed exponentially with a lifetime (21 ps) that compares favorably with the lifetime of the slower component (22 ps) of the recovery of the negative absorption centered at 740 nm. As discussed above, it could be that this 21 ps component of recovery of absorption at 740 nm is actually the growth of positive absorption at this wavelength arising from the LMCT state, or it could indeed be a true ground-state repopulation process. If the latter is the case, then it is necessary to conclude that the (d,d) state decays to the ground-state surface in parallel with its decay into the LMCT state. Unlike in the case of the FOT, it is not possible on the present evidence to determine whether there is branching in the decay of the (d,d) state, or whether it converts to the LMCT state with unit efficiency.

The final question to be addressed is whether the possible conformational excursion of the complex from one saddled conformation through the planar "maximum" to the opposite saddled structure might lead to a somewhat different interpretation of the ultrafast experiments. The TDDFT results for the flat geometry (D_{4h} in the ground state) show that the major effect of flattening the molecule is to lower the $^3(d_{z^2},d_{x^2-y^2})$ and ^{1,3}LMCT excited states. In the D_{4h} molecule, the $^3(d_{z^2},d_{x^2-y^2})$ (1^3B_{1g}) is predicted to lie adiabatically below the $^1(\pi,\pi^*)$ (1^1E_u). So is the ^{1,3}LMCT ($1^{1,3}B_{1u}$) pair with respect to the $^3(\pi,\pi^*)$ (1^3E_u). This suggests that, in the case the molecule flattens, the primarily excited S_1 (π,π^*) deactivates in a cascade of events, populating in turn the $^3(d_{z^2}, d_{x^2-y^2})$ and the ^{3}LMCT states, before finally regaining the ground-state surface.

The studies presented here on NiPc(BuO)$_8$ point to an important role of the $^3(d_{z^2},d_{x^2-y^2})$ state, suggesting a resemblance of the radiationless deactivation mechanism of NiPcs to the one in nickel porphyrins such as NiOEP and NiTPP.[10−19] We should however caution that there are significant differences between these compounds. In NiPcs, due to the upshift of the G-a_{1u}, the ^{1,3}LMCT states involving excitations out of the G-a_{1u} into the Ni-$d_{x^2-y^2}$ MO are sufficiently low in energy to provide effective routes for radiationless deactivation of the $^{1,3}(\pi,\pi^*)$ states. The (d,d) ligand field states, which are crucial intermediates in the deactivation of photoexcited low-spin d^8 nickel porphyrins, do not necessarily play such a dominant role in the photophysics of nickel phthalocyanines. In NiPcs, the $S_1(\pi,\pi^*)$ state is red shifted and the $^3(d_{z^2},d_{x^2-y^2})$ ligand field state is blue shifted with respect to the porphyrin analogues. Therefore, if the primarily excited $S_1(\pi,\pi^*)$ state lies at too long wavelengths, as in NiNc(BuO)$_8$ where the Q-band lies at 850 nm,[6] the $^3(d_{z^2},d_{x^2-y^2})$ might not be involved at all in the radiationless decay. Or, as found here for NiPc(BuO)$_8$, it intervenes only at the early stage of the decay process.

Conclusions

The excited-state spectral and dynamic behavior of NiPc(BuO)$_8$ in toluene were investigated by ultrafast transient absorption spectroscopy and interpreted in the light of DFT/TDDFT theoretical studies. NiPc(BuO)$_8$ was shown to have a highly saddled structure in the crystalline state. In solution the theoretical results indicated that it can flap from one D_{2d}-saddled conformation to the opposite one through a D_{4h}-planar structure. Under pulsed photoexcitation at 735 nm, the most prominent features in the transient spectrum of the complex in toluene were positive absorption bands having $\lambda_{max} = 625$ and 760 nm, and a negative absorption (bleaching) in the wavelength region of the ground-state absorption maximum with $\lambda_{min} = 735$ nm, and a weaker band with $\lambda_{min} = 655$ nm. In the case of the 760 nm positive band, the absorption maximum shifted over the first 5 ps, or so. Taken together with the indications from the theoretical studies, the spectral and kinetic changes for the complex in toluene can be understood in terms of the 730 nm excitation light generating a primarily excited S_1 (π,π^*) state that transforms initially into a vibrationally hot $^3(d_{z^2},d_{x^2-y^2})$ state. Cooling to the zeroth state is complete after ca. 8 ps. The cold (d,d) state converted to its daughter state, the ^{3}LMCT ($\pi,d_{x^2-y^2}$), which itself decays to the ground state with a lifetime of 640 ps. Population of the $^3(\pi,\pi^*)$ through the decay of the ^{3}(d,d) state cannot be ruled out, but if so the only nonradiative decay route for this state is to the LMCT state, so the net result would be the same as if the $^3(\pi,\pi^*)$ did not intervene. The excited-state calculations indicate that the proposed deactivation mechanism applies to the D_{2d}-saddled and the D_{4h}-planar structure as well.

Acknowledgment. The experimental studies conducted at the Ohio Laboratory for Kinetic Spectrometry (BGSU) were supported in part by NIH Grant CA 91027 and by an instrumentation grant from the Hayes Investment Foundation (Ohio Board of Regents). A.R. and G.R. thank the Italian MIUR (Ministero dell' Istruzione, dell' Università e della Ricerca) and the Università della Basilicata, Italy for support (Grant 2003038084_002). T.C.G. expresses gratitude to the McMaster Foundation (BGSU) for a pre-doctoral fellowship.

Supporting Information Available: ORTEP top view of the **NiPc(BuO)$_8$** complex, data collection and structure refinement details, tables giving crystal data, atomic coordinates, isotropic and anisotropic displacement parameters, and bond length and angles. This material is available free of charge via Internet at http://pub.acs.org. Full X-ray structural information is available as an X-ray crystallographic file in CIF format. CIF has been submitted to the CCDC with entry number CCDC 237068. This material is available free of charge via the Internet at http://pubs.acs.org.

References and Notes

(1) Wagner, R. W.; Lindsey, J. S.; Seth, J.; Palaniappan, V.; Bocian, D. F. *J. Am. Chem. Soc.* **1996**, *118*, 3996.

(2) Reimers, J. R.; Lü, T. X.; Crossley, M. J.; Hush, N. S. *Chem. Phys. Lett.* **1996**, *256*, 353.

(3) *Phthalocyanines: Properties and Applications*; Leznoff, C. C.; Lever, A. B. P., Eds.; VCH Publishers: New York, 1990−1996; Vols. 1−4.

(4) Fernández, D. A.; Awruch, J.; Dicelio, L. E. *Photochem. Photobiol.* **1996**, *63*, 784.

(5) Lawrence, D. S.; Whitten, D. G. *Photochem. Photobiol.* **1996**, *64*, 923.

(6) Busetti, A.; Soncin, M.; Reddi, E.; Rodgers, M. A. J.; Kenney, M. E.; Jori, G. *J. Photochem. Photobiol. B: Biol.* **1999**, *53*, 103.

(7) Retsek, J. L.; Drain, C. M.; Kirmaier, C.; Nurco, D. J.; Medforth, C. J.; Smith, K. M.; Sazanovich, I. V.; Chirvony, V. S.; Fajer, J.; Holten, D. *J. Am. Chem. Soc.* **2002**, *125*, 9787.

(8) Antipas, A.; Gouterman, M. *J. Am. Chem. Soc.* **1983**, *105*, 4896.

(9) Gouterman, M. The Porphyrins. In *The Porphyrins*; Dolphin, D., Ed.; Academic Press: New York, 1978; Vol. 3, p 1.

(10) Rodriguez, J.; Holten, D. *J. Chem. Phys.* **1989**, *91*, 3525.

(11) Rodriguez, J.; Kirmaier, C.; Holten, D. *J. Am. Chem. Soc.* **1989**, *111*, 6500.

(12) Rodriguez, J.; Kirmaier, C.; Holten, D. *J. Chem. Phys.* **1991**, *94*, 6020.

(13) Kobayashi, T.; Straub, K. D.; Rentzepis, P. M. *Photochem. Photobiol.* **1979**, *29*, 925.

(14) Chirvony, V. S.; Dzhagarov, B. M.; Timinskii, Y. V.; Gurinovich, G. P. *Chem. Phys. Lett.* **1980**, *70*, 79.

(15) Kim, D.; Kirmaier, C.; Holten, D. *Chem. Phys.* **1983**, *75*, 305.

(16) Kim, D.; Holten, D. *Chem. Phys. Lett.* **1983**, *98*, 584.

(17) Chikisev, A. Y.; Kamalov, V. F.; Korteev, N. I.; Kvach, V. V.; Shkvrinov, A. P.; Toluetaev, B. N. *Chem. Phys. Lett.* **1988**, *144*, 90.

(18) Apanasevich, P. A.; Kvach, V. V.; Orlovich, V. A. *J. Raman Spectrosc.* **1989**, *20*, 125.

(19) Sato, S.; Kitiagawa, T. *Appl. Phys.* **1994**, *B59*, 415.

(20) Rosa, A.; Baerends, E. J. *Inorg. Chem.* **1993**, *32*, 5637.

(21) Rosa, A.; Baerends, E. J. *Inorg. Chem.* **1994**, *33*, 584.

(22) Rosa, A.; Ricciardi, G.; Baerends, E. J.; van Gisbergen, S. J. A. *J. Phys. Chem. A* **2001**, *105*, 3311.

(23) Altomare, A.; Burla, M. C.; Camalli, M.; Cascarano, G.; Giacovazzo, C.; Guagliardi, A.; Moliterni, A. G. G.; Polidori, G.; Spagna, R. *J. Appl. Crystallogr.* **1999**, *32*, 115.

(24) Sheldrick, G. M. SHELXL93; University of Göttingen, Göttingen, Germany, 1993.

(25) Nikolaitchik, A. V.; Korth, O.; Rodgers, M. A. J. *J. Phys. Chem. A* **1999**, *103*, 7587.

(26) Pelliccioli, A. P.; Henbest, K.; Kwag, G.; Carvagno, T. R.; Kenney, M. E.; Rodgers, M. A. J. *J. Phys. Chem. A* **2001**, *105*, 1757.

(27) Baerends, E. J.; Ellis, D. E.; Ros, P. *Chem. Phys.* **1973**, *2*, 41.

(28) te Velde, G.; Baerends, E. J. *J. Comput. Phys.* **1992**, *99*, 84.

(29) Fonseca Guerra, C.; Snijders, J. G.; te Velde, G.; Baerends, E. J. *Theor. Chem. Acc.* **1998**, *99*, 391.

(30) Vosko, S. H.; Wilk, L.; Nusair, M. *Can. J. Phys.* **1980**, *58*, 1200.

(31) Becke, A. *Phys. Rev. A* **1988**, *38*, 3098.

(32) Perdew, J. P. *Phys. Rev. B* **1986**, *33*, 8822 (Erratum: *Phys. Rev. B* **1986**, *34*, 7406).

(33) van Gisbergen, S. J. A.; Snijders, J. G.; Baerends, E. J. *Comput. Phys. Commun.* **1999**, *118*, 119.

(34) van Gisbergen, S. J. A.; Snijders, J. G.; Baerends, E. J. *J. Chem. Phys.* **1995**, *103*, 9347.

(35) Schaftenaar, G.; Noordik, J. H. *J. Comput.-Aided Mol. Des.* **2000**, *14*, 123.

(36) Volkov, A. V. Ph.D. Thesis, State University of New York at Buffalo, New York, 1999.

(37) Gardberg, A. S.; Sprauve, A. E.; Ibers, J. A. *Inorg. Chim. Acta* **2002**, *328*, 179.

(38) Kasuga, K.; Kawashima, M.; Asano, K.; Sugimori, T.; Abe, K.; Kikkawa, T.; Fujiwara, T. *Chem. Lett.* **1996**, 867.

(39) Kasuga, K.; Asano, K.; Lin, T.; Sugimori, T.; Handa, M.; Abe, K.; Kikkawa, T.; Fujiwara, T. *Bull. Chem. Soc. Jpn.* **1997**, *70*, 1859.

(40) Helliwell, M.; Deacon, A.; Moon, K. J.; Powell, A. K.; Cook, M. J. *Acta Crystallogr. B* **1997**, *53*, 231.

(41) What we call LMCT transitions are not really ligand-to-metal CT transitions, the classification in terms of LMCT used here being merely based on the character of the orbitals involved in the transitions. In fact, a thoroughly analysis of the changes in Mulliken population accompanying the $1^1A_1(GS) \rightarrow 1^{1,3}A_2(LMCT)$ transitions reveals that no net charge-transfer occurs from the ligand to the metal, but only a reorganization of the electronic density, that happens quite frequently in the so-called LMCT states of transition metal complexes (for an extensive discussion on this topic, see ref 42). Therefore, the well-known failure of TDDFT in predicting the excitation energies of long-range charge-transfer states correctly (see refs 43−46) does not occur here, and one can trust the TDDFT energies calculated for the $1^{1,3}A_2(LMCT)$ states.

(42) Rosa, A.; Ricciardi, G.; Gritsenko, O.; Baerends, E. J. *Struct. Bond.* **2004**, *112*, 49.

(43) Casida, M. E.; Gutierrez, F.; Guan, J.; Gadea, F.-X.; Salahub, D.; Daudey, J.-P. *J. Chem. Phys.* **2000**, *113*, 7062.

(44) Dreuw, A.; Weisman, J. L.; Head-Gordon, M. *J. Chem. Phys.* **2003**, *119*, 2943.

(45) Dreuw, A.; Head-Gordon, M. *J. Am. Chem. Soc.* **2004**, *126*, 4007.

(46) Gritsenko, O.; Baerends, E. J. *J. Chem. Phys.* **2004**, *112*, 655.